

pubs.acs.org/acscatalysis Research Article

Oxygen Reduction Electrocatalysis with Epitaxially Grown Spinel MnFe₂O₄ and Fe₃O₄

Alexandria R. C. Bredar, [⊥] Miles D. Blanchet, [⊥] Andricus R. Burton, Bethany E. Matthews, Steven R. Spurgeon, Ryan B. Comes, * and Byron H. Farnum*



Cite This: ACS Catal. 2022, 12, 3577-3588



ACCESS I

Metrics & More

Article Recommendations

s Supporting Information

ABSTRACT: Nanocrystalline $MnFe_2O_4$ has shown promise as a catalyst for the oxygen reduction reaction (ORR) in alkaline solutions, but the material has been sparingly studied as highly ordered thin-film catalysts. To examine the role of surface termination and Mn and Fe site occupancy, epitaxial $MnFe_2O_4$ and Fe_3O_4 spinel oxide films were grown on (001)- and (111)-oriented Nb:SrTiO₃ perovskite substrates using molecular beam epitaxy and studied as electrocatalysts for the oxygen reduction reaction (ORR). High-resolution X-ray diffraction (HRXRD) and X-ray photoelectron spectroscopy (XPS) show the synthesis of pure phase materials, while scanning transmission electron microscopy (STEM) and reflection high-energy electron diffraction (RHEED) analysis demonstrate island-like growth of (111) surface-terminated pyramids on both (001)- and (111)-oriented substrates, consistent with the literature and attributed to the lattice mismatch between the spinel films and the perovskite substrate. Cyclic voltammograms under a N_2 atmosphere revealed



Top View of RDE Tip

Side View of Electrode

- ✓ Electrode Design Suitable for RDE Experiments
- ✓ Diffusion-Limited Current Observed
- ✓ Selectivity for 4e- ORR

distinct redox features for Mn and Fe surface termination based on comparison of MnFe₂O₄ and Fe₃O₄. Under an O₂ atmosphere, electrocatalytic reduction of oxygen was observed at both Mn and Fe redox features; however, a diffusion-limited current was only achieved at potentials consistent with Fe reduction. This result contrasts with that of nanocrystalline MnFe₂O₄ reported in the literature where the diffusion-limited current is achieved with Mn-based catalysis. This difference is attributed to a low density of Mn surface termination, as determined by the integration of current from CVs collected under N₂, in addition to low conductivity through the MnFe₂O₄ film due to the degree of inversion. Such low densities are attributed to the synthetic method and island-like growth pattern and highlight challenges in studying ORR catalysis with single-crystal spinel materials.

KEYWORDS: ORR catalysis, spinel oxides, MnFe₂O₄, Fe₃O₄, molecular beam epitaxy

■ INTRODUCTION

The use of fuel cells in our changing energy economy relies heavily on Pt as an oxygen reduction catalyst, which is costly for the widespread use of this technology. The exploration of new materials that are cheaper and more abundant is therefore important for the use and expansion of fuel cells. The catalysis of the oxygen reduction reaction (ORR) is complicated by its sluggish kinetics, which results from the need for O₂ to adsorb to the surface of the catalyst, break the O=O (498 kJ mol⁻¹) double bond, and then desorb from the surface, all of which may involve several different peroxides or hydroxide intermediates.^{2,3} There are two pathways for ORR in alkaline conditions known as the 4-electron (eq 1) and 2×2 -electron pathways (eq 2). The 4-electron pathway is thermodynamically more favorable due to the more efficient conversion of O2 and the avoidance of peroxide side products produced by the 2 × 2-electron pathway, which can be detrimental to other components of fuels cells.4 The challenges of finding alternative catalysts to Pt lie in materials that not only have similar overpotentials but also have similar selectivity for the 4electron pathway.

$$O_2 + 2H_2O + 4e^- \rightarrow 4OH^- \quad E^o = 1.23 \text{ V vs RHE} \quad (1)$$

$$O_2 + H_2O + 2e^- \rightarrow HO_2^- + OH^- \quad E^o = 0.73 \text{ V vs RHE}$$

$$HO_2^- + H_2O + 2e^- \rightarrow 3OH^ E^0 = 1.74 \text{ V vs RHE}$$
 (2)

Spinel oxides have emerged as attractive alternative catalysts for the ORR due to their versatility and tunability of their reactivity depending on the chemical nature of their metal cations. Spinel oxides are ternary materials with the chemical formula AB_2O_4 , where the A cation is typically in the 2+ oxidation state and the B cation is typically in the 3+ oxidation state. Depending on the identity of the metal cations, A and B cations may occupy tetrahedral or octahedral sites ranging

Received: November 10, 2021 Revised: February 23, 2022



from normal (A^{tet}B₂^{oct}O₄) to inverse (A^{oct}B^{tet}B^{oct}O₄) structures. Many elements can be incorporated into the spinel structure, giving a large library of materials to explore.⁵

In terms of low cost and abundance, first-row transition metals have been heavily explored as nanomaterials for the ORR, and almost all of the first-row transition-metal spinels show some propensity toward ORR, with some even demonstrating onset potentials that are competitive with Pt.6 The ability of these materials to perform ORR lies in the oxidation state promiscuity and the occupation of different coordination sites within the spinel structure. Co, Fe, and Mn, for example, all have at least two different thermodynamically possible oxidation states that can be utilized when catalyzing the ORR, which is important for charge balance and electron transfer when performing catalysis. Studies of ORR catalysis with spinels have also shown that the occupation of octahedral or tetrahedral sites for different cations can change the catalyst's ability to perform the ORR.^{8,9} Several studies of ferrite-based spinels (AFe2O4, where A is Co, Fe, Mn, Ni, or Cu) have been performed with Co and Mn ferrite spinels showing the best ORR activity. 6,10-16 However, differences in the synthetic method of nanocrystals and evaluation of ORR make the determination of an outright champion difficult.

The exploration of almost all ORR spinel catalysts has typically been done with nanocrystalline materials on a carbon support. The carbon support is important because it enhances the conductivity and stability of the metal oxide catalyst. However, carbon support materials have also been shown to perform ORR without a transition-metal catalyst, albeit less efficiently. The complexities of carbon support/oxide nanocrystal composites make it difficult to understand the contribution of just the spinel metal oxide to the ORR and its true catalytic activity. Understanding the intrinsic thermodynamics and the kinetics of the ORR on spinel metal oxide surfaces is important to understanding their catalytic mechanism and realizing their full potential as alternative catalysts to Pt.

To study the surface of a catalyst in greater detail, the use of single-crystalline materials is beneficial. ORR catalysis using single-crystal Pt, Pd, and Ag has all been achieved, which allows for an understanding of catalysis at a specific surface termination. 19-21 These materials are also readily available as substrates that configure well into electrodes for rotating disk electrochemistry (RDE) experiments typically used to study the ORR. Perovskite oxides, such as $LaMO_3$ (where M = Fe, Co, Mn, and Ni as a few examples), have also been grown epitaxially and studied for the ORR; however, the electrode configuration in most of these studies either prevented RDE experiments from being performed 22,23 or was more relevant to solid oxide fuel cell devices.^{24,25} In terms of perovskite oxides, only one study by Kan et al. used RDE to study La_{0.66}Sr_{0.33}MnO₃ grown on the conductive perovskite substrate Nb:SrTiO3 and found that a diffusion-limited current could not be achieved.²⁶

A recent study by Yang et al. explored epitaxial thin-film ferrite spinels in an RDE configuration for ORR electrocatalysis. Fe_3O_4 and Co-doped Fe_3O_4 were grown on MgO substrates and studied electrocatalytically in a configuration where contact was made to the front of the films. While their configuration showed valid RDE measurements with Pd thin films, they were not able to reach the diffusion-limited current with their spinel films and overall achieved low current densities, most likely due to limitations of lateral charge

transport through the spinel thin film. To our knowledge, this is the only other report in the literature that describes ORR electrocatalysis at an epitaxial spinel oxide film.²⁷

Herein, we describe our study of epitaxially grown MnFe $_2O_4$ and Fe $_3O_4$ for ORR electrocatalysis, which has been studied significantly as nanocrystalline catalysts. 6,11,14,28,29 The epitaxial films were prepared using molecular beam epitaxy (MBE). MnFe $_2O_4$ has been grown epitaxially using MBE previously but not specifically for the study of ORR catalysis. Nb:SrTiO $_3$ (Nb:STO) perovskite substrates were used for oxide growth because of their high conductivity and the current unavailability of conductive spinel substrates. Once grown, the films were made into electrodes for RDE measurements, as shown in Figure 1.

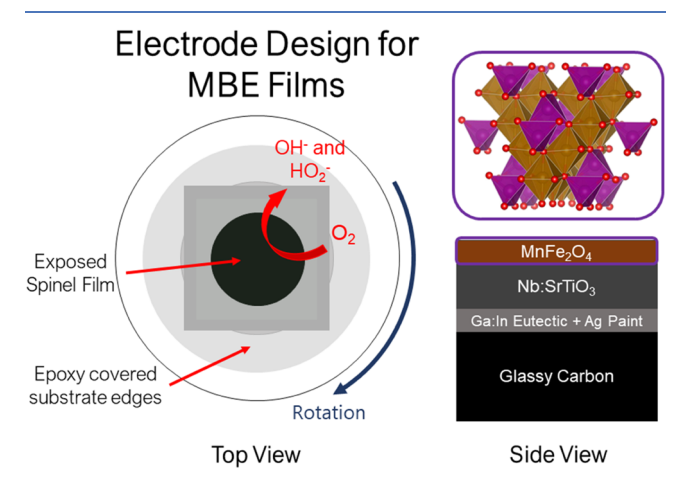


Figure 1. Diagram of the electrode used to study ferrite spinel epitaxial films for ORR catalysis.

This is the first study to our knowledge of MnFe₂O₄ and Fe₃O₄ grown on a perovskite substrate used for electrocatalysis and provides insight into the specific mechanism through which MnFe₂O₄ and Fe₃O₄ catalyze the ORR. In this study, MnFe₂O₄ and Fe₃O₄ were grown on (001)- and (111)oriented Nb:STO to study the effect of surface termination on the film growth and catalysis. Films of varying thicknesses were also studied. We find that the diffusion-limited current consistent with the 4-electron mechanism can be reached in an O₂-saturated electrolyte. Interestingly, the overpotential at which this current is achieved (-0.1 V vs RHE, $\eta_{ORR} = 1.33 \text{ V}$) is consistent with the reduction of Fe sites in the crystal structure, while the catalytic current at Mn sites, occurring at smaller overpotentials (0.65 V, η_{ORR} = 0.58 V), was much lower. This result runs counter to those observed for nanocrystalline electrodes where the diffusion-limited current is achieved through Mn site catalysis. We hypothesize that this discrepancy is due to a combination of low Mn surface density on the {111} island facets that form on the perovskite substrate and low conductivity of MnFe₂O₄.

■ EXPERIMENTAL SECTION

Synthesis of MnFe₂O₄ and Fe₃O₄ Films. MnFe₂O₄ films were grown on either (001)-oriented or (111)-oriented niobium-doped SrTiO₃, (Nb:STO, 0.7 wt %, MTI Crystal), conductive perovskite substrates using molecular beam epitaxy (MBE, Mantis Deposition). Substrates were sonicated in acetone (ACS Grade, VWR) and isopropyl alcohol (ACS Grade, VWR) for \sim 5 min each before being loaded into the

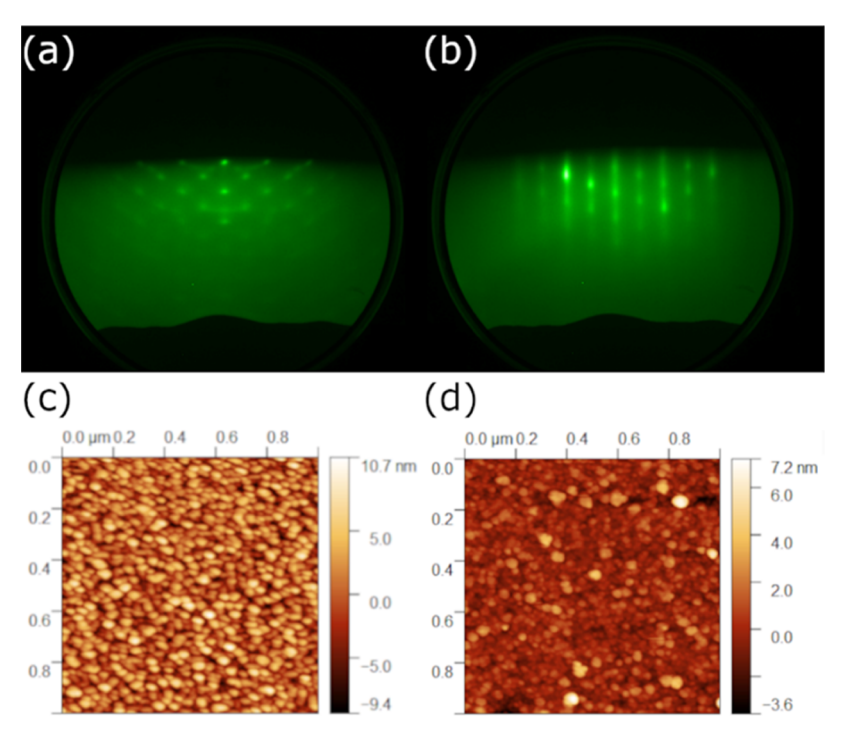


Figure 2. RHEED and AFM images of (a, c) 6 nm (001) MnFe₂O₄ and (b, d) 6 nm (111) MnFe₂O₄.

MBE chamber. Elemental Mn (99.95%, ACI Alloys) and Fe (99.98%, Sigma-Aldrich) were deposited concurrently during growth, while effusion cells were kept at a constant temperature, with deposition rates calibrated using a quartz-crystal microbalance (QCM) pre-growth. The sample stage was heated to a constant temperature using an infrared ceramic heating source and measured via a thermocouple on the stage, which causes an overestimation of ~50 to 100 °C relative to the substrate surface temperature. Samples were grown at 525 °C setpoints and subsequently cooled to ambient temperatures over ~30 min. O_2 gas was introduced into the chamber and maintained at ~7.0 × 10^{-6} Torr during the growth and cooling of films. Fe₃O₄ was grown at the same conditions on (001)-oriented Nb:STO, except that the O_2 gas pressure was maintained at ~4.5 × 10^{-6} Torr.³¹

Characterization of MnFe₂O₄ and Fe₃O₄ Films. Reflection high-energy electron diffraction (RHEED), a technique sensitive to the first few atomic layers of a film surface, was used to monitor the growth process. After growth, samples were analyzed using X-ray photoelectron spectroscopy (XPS, PHI 5400 refurbished by RBD Instruments). The XPS system was connected to the MBE chamber by a vacuum transfer line to prevent atmospheric contamination. A monochromatic Al Ka X-ray source, an electron pass energy of 35.75 eV, and a scanning step size of 0.05 eV were used for all samples. The conductivity of the Nb:STO substrates negated the need for an electron emission neutralizer for sample charge compensation. All spectra were shifted accordingly to place their Fe 2p_{3/2} peaks at a 711 eV binding energy. 32,33 Atomic force microscopy (AFM) was used to acquire images of film topography and was acquired using a Park XE7 AFM in a noncontact mode. Out-of-plane highresolution X-ray diffraction (HRXRD) and X-ray reflectivity (XRR) were performed using a Rigaku SmartLab system (Cu $K\alpha$ source) with a hybrid pixel area detector in a 0D mode.

Cross sectional scanning transmission electron microscopy (STEM) samples were prepared using an FEI Helios NanoLab DualBeam Ga⁺ Focused Ion Beam (FIB) microscope with a standard lift-out procedure. STEM high-angle annular dark-field (STEM-HAADF) images were collected on a probe-corrected JEOL GrandARM-300F microscope operating at 300 kV, with a convergence semiangle of 29.7 mrad and a collection angle range of 75–515 mrad. STEM energy-dispersive X-ray spectroscopy (STEM-EDS) maps were acquired using a dual JEOL Centurio silicon drift detector setup and were processed for the Fe K, Mn K, Sr L, and Pt M peaks.

Electrocatalytic Studies of MnFe₂O₄ and Fe₃O₄ Films. Electrodes were constructed from MnFe₂O₄ and Fe₃O₄ films by mounting films on RDE tips with a glassy carbon (GC) disk working electrode (Pine Research, 5 mm diameter) as the contact material, as shown in Figure 1. The electrode was constructed using Ga:In eutectic (99.99%, Sigma-Aldrich) and silver paint (Ted Pella). A drop of Ga:In eutectic was placed in the middle of the GC electrode to make the electrical contact to the backside of the Nb:STO. Before the film was placed, a ring of Ag paint was placed around the eutectic and was used as a conductive adhesive, so the film would adhere to the glassy carbon surface while keeping the eutectic in place. The film was placed on the eutectic and paint and allowed to dry for 30 min. Once the film could not be moved with gentle pressure, an inert epoxy (Loctite D-609) was used to cover the film, making sure any exposed GC, eutectic, and Ag paint are covered so they did not interfere with electrochemical measurements. The epoxy was placed such that the edge of the Nb:STO substrate was covered as well, leaving only the exposed MnFe₂O₄ film. The epoxy was then left to dry at room temperature for at least 24 h before the electrode was used for electrocatalysis. The final area of the exposed film was measured using ImageJ software, and all CVs and RDE measurements were normalized to the geometric area of the exposed film measured from Image].

All electrochemical measurements were performed in 0.1 M KOH as the electrolyte. A Hg/HgO reference electrode was used and checked against ferricyanide for every experiment for accurate conversion to RHE, in which all potentials are reported against. All cyclic voltammetry (CV) and RDE experiments were performed using a WaveDriver 20 bipotentiostat (Pine Research) with an MSR rotator (Pine Research). For noncatalysis electrochemistry, N₂ (UHP 99.999%, Airgas) was purged into the solution for at least 30 min. For ORR measurements, O₂ (UHP 99.999%, Airgas) was purged into the solution for at least 30 min. To confirm that our electrode design was applicable for rotation studies, a Pt disk electrode with a similar epoxy coating to our MBE electrodes was tested under ORR conditions.

RESULTS

MBE Synthesis and Characterization. MnFe₂O₄ and Fe₃O₄ spinel films were grown on 10 mm × 10 mm Nb:STO substrates and then subsequently diced into 5 mm × 5 mm pieces so that different methods of characterization could be performed. Experiments were performed on four different spinel films: 6 nm MnFe₂O₄ grown on (001) Nb:STO, 16 nm MnFe₂O₄ on (001), 6 nm MnFe₂O₄ on (111) Nb:STO, and 21 nm Fe₃O₄ on (001) Nb:STO. Initial assurance of successful growth was observed with in situ RHEED analysis, which can determine the crystallinity and surface morphology of the material based on the scattering of electrons from the film surface. Figure 2a,b shows RHEED analysis of 6 nm (001) and 6 nm (111) MnFe₂O₄ for a direct comparison of the impact of substrate orientation. Films grown on (001)-oriented Nb:STO revealed a (001)-oriented spinel structure with an island decorated surface, while those grown on (111)-oriented Nb:STO showed a (111)-oriented spinel structure with smaller island features and a more planar surface quality. These results are indicated by the spotted pattern for MnFe₂O₄ grown on the (001) substrate, as opposed to the pattern with vertical streaks combined with spots for the film grown on the (111) substrate. The RHEED pattern for films grown on (001) substrates was the same regardless of thickness, with the RHEED for 16 nm MnFe₂O₄ and 21 nm Fe₃O₄ on (001) Nb:STO, as shown in Figure S1. For all films used in this study, the RHEED patterns obtained during growth showed little change over time, indicating that the orientations were uniform throughout the epitaxial films. The island growth results are typical for spinel ferrites grown on Nb:STO, where there is a significant lattice mismatch (\sim 7%) between the MnFe₂O₄ film lattice parameter ($a/2 \approx 4.24 \text{ Å}$) and that of the substrate (a = 3.905 Å). The {111}-type surfaces are also the minimum energy surface for spinel films,³⁴ which leads to faceting into pyramid-type islands when grown on a (001) substrate. This Volmer-Weber growth mode has been observed previously for CoFe₂O₄ films grown on STO.³⁵

AFM analysis shown in Figure 2c,d further verified the RHEED results, as the root mean square roughness for the 6 nm (001) MnFe₂O₄ film was greater at 3.2 ± 0.5 nm compared to 1.0 ± 0.5 nm for the 6 nm (111) film. AFM for 16 nm (001) MnFe₂O₄ and for 21 nm (001) Fe₃O₄ is shown in Figure S1. The reduction in the surface roughness on (111) Nb:STO reflects the smoother surface seen in RHEED and is also expected given that surface faceting would be reduced since the (111) surface is already the minimum energy surface for spinel

oxides. In all cases, residual film strain is fully relaxed to the bulk value due to this island growth mode.

Out-of-plane HRXRD results for the films are shown in Figure 3. $MnFe_2O_4$ (Fe_3O_4) grown on (001) substrates

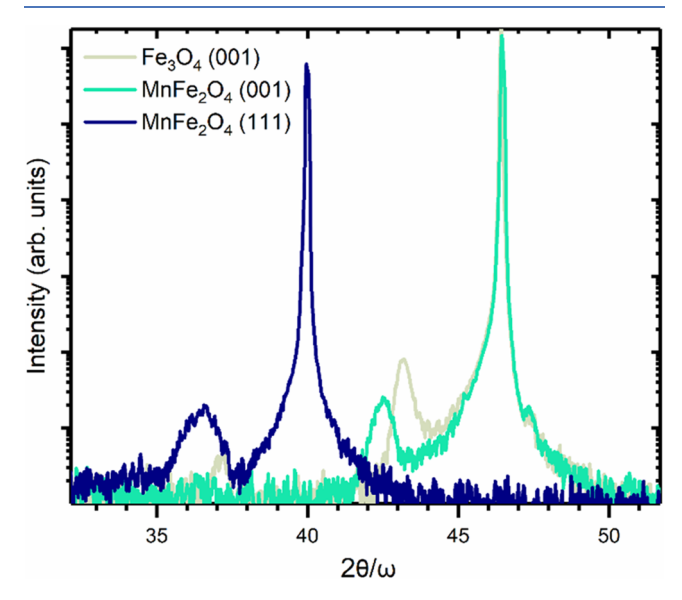


Figure 3. HRXRD diffractogram of 21 nm Fe $_3O_4$ grown on (001)-, 16 nm MnFe $_2O_4$ grown on (001)-, and 6 nm grown on (111)-oriented Nb:STO substrates. Large peaks at 40.0 and 46.4° indicate the (111) and (002) lattice planes of the Nb:STO substrate. Smaller peaks at 36.6, 42.5, and 43.3° are consistent with (222) MnFe $_2O_4$, (004) MnFe $_2O_4$, and (004) Fe $_3O_4$ lattice planes. The vertical axis is on an arbitrary log scale.

showed a peak at 42.5° (43.3°) consistent with a (004) lattice peak of the spinel film, close to the (002) Nb:STO substrate peak at 46.4°. MnFe₂O₄ grown on (111) Nb:STO showed a (222) film peak at 36.6°, close to the (111) substrate peak at 40.0°. C-lattice parameters of the MnFe₂O₄ (Fe₃O₄) film were calculated to be 8.50(1) Å (8.35(1) Å) and the distance between (111) planes of MnFe₂O₄ to be 4.91(1) Å. These parameters are consistent with those found in the literature for $MnFe_2O_4$ and Fe_3O_4 spinels. ^{36,37} The film thickness for MnFe₂O₄ grown on (111) Nb:STO was determined using an XRR fit (Figure S2), but this could not be done for films grown on (001) substrates due to their significantly higher surface roughness. Thicknesses of (001)-oriented films were calculated by comparing the composition, QCM calibration rates, and growth time between samples, while using the thickness of MnFe₂O₄ grown on (111) Nb:STO as a reference. Thicknesses calculated using QCM data have an uncertainty of ± 1 nm.

STEM analysis of the 6 nm (001) MnFe₂O₄ film was performed before and after electrochemical experiments to assess possible microstructural and composition changes, as shown in Figure 4. Cross sectional STEM-HAADF images for the film prior to electrochemical experiments revealed a distinct island morphology with clear {111}-type faceting, consistent with RHEED images, and a thin (<3 nm thick) uniform bridging layer between islands on the substrate surface. STEM-EDS maps of Fe, Mn, Sr, and Pt are shown in Figure 4c, which reveal a sharp film—substrate interface and uniform island composition. Figure 4i shows a high magnification of the interface region and highlights the crystallinity of the MnFe₂O₄ layer and surface faceting.

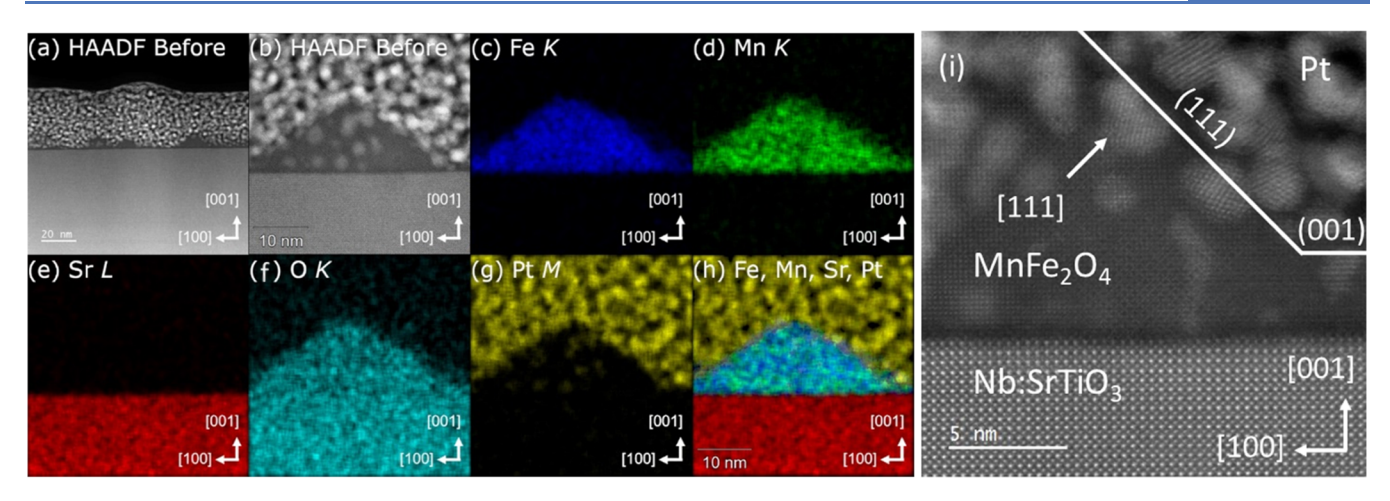


Figure 4. Cross sectional low-magnification (a) and high-magnification (b) STEM-HAADF images of a 6 nm (001)-oriented $MnFe_2O_4$ film along with elemental (c-g) and composite (h) STEM-EDS maps collected before cycling. (i) High-resolution image of the Nb:STO/MnFe₂O₄ interface showing crystallinity and surface faceting. White contrast regions indicate the Pt deposition overlayer.

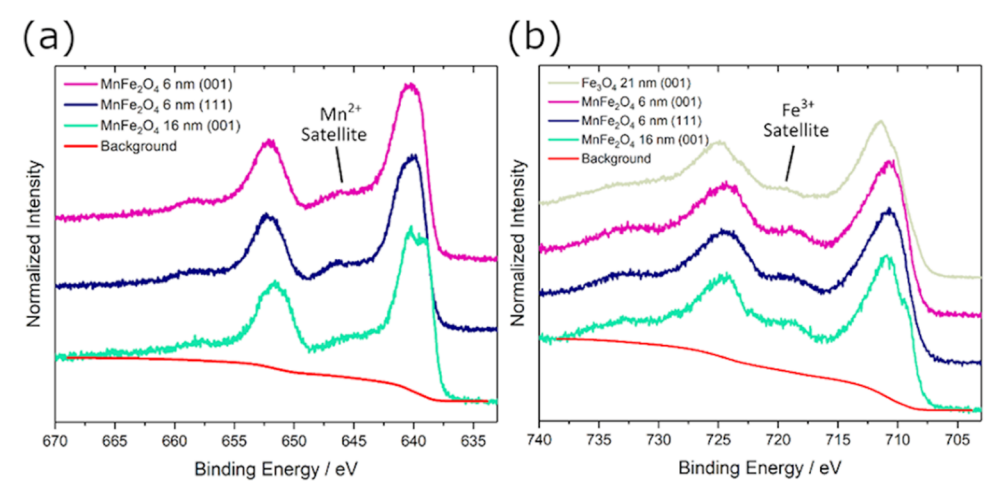


Figure 5. XPS of the (a) Mn 2p region and (b) Fe 2p region for 6 nm (001), 6 nm (111), and 16 nm (001) MnFe₂O₄. Also includes 21 nm (001) Fe₃O₄.

STEM data collected post-catalysis is discussed after electrocatalytic data are presented.

XPS analysis of the films was performed to characterize their composition, including stoichiometry and metal oxidation states. XPS data for the Mn 2p and Fe 2p regions are shown in Figure 5 with stoichiometry results presented in Table 1. The

Table 1. Stoichiometry from XPS

$MnFe_2O_4$ film	Mn atom %	Fe atom %	Mn/Fe
6 nm (001) vacuum	38	62	0.61
6 nm (111) vacuum	34	66	0.52
16 nm (001) vacuum	31	69	0.45

percentages shown in Table 1 are based on the total metal content excluding oxygen. It should be noted that all spectra were normalized, so the absolute peak intensity is unrelated to stoichiometry. The Mn and Fe stoichiometry for samples still under vacuum was determined by comparing areas of the Mn 2p and Fe 2p regions after implementing a Shirley background subtraction and sensitivity factors of 2.42 and 2.686 for Mn and Fe, respectively. Stoichiometry determination from XPS for samples that were exposed to atmospheric conditions was not considered since the 2p region backgrounds varied greatly

due to the effects of atmospheric contamination. The stoichiometry of the films under vacuum varied from sample to sample, with both 6 nm films showing a slight Mn excess and the 16 nm film showing a slight Mn deficiency. A perfect MnFe₂O₄ spinel composition should be 33.3% Mn and 66.7% Fe. Values shown in Table 1 are close to the theoretical estimate; however, reliable stoichiometry determination from XPS is difficult without MnFe₂O₄ standards. Concentrations determined from XPS using the background shown in Figure 5 should be considered as an upper bound for Mn and a lower bound for Fe. EDS analysis was also performed on each film after removal from vacuum to obtain comparative stoichiometry. These data are presented in Table S1 and show similar estimates to XPS but with slightly smaller Mn atom % and larger Fe atom %. In terms of oxidation state, all MnFe₂O₄ samples under vacuum showed similar spectral features, indicating that the oxidation states of the Mn and Fe were consistent across the films. The Mn $2p_{3/2}$ peaks, located around 640 eV, have satellite peaks around 645 eV, which indicates a $\rm Mn^{2+}$ oxidation state. The Fe $\rm 2p_{1/2}$ peaks of $\rm MnFe_2O_4$, positioned around 725 eV, have a satellite peak (\sim 720 eV), which indicates a Fe³⁺ oxidation state.³⁹ The Fe 2p spectrum of the Fe₃O₄ film shows mixed 2+ and 3+ oxidation

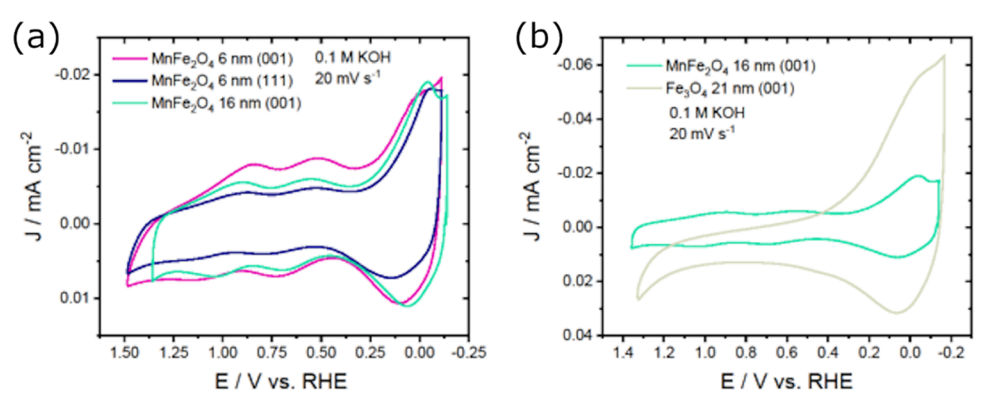


Figure 6. (a) CVs comparing MnFe₂O₄ films grown on (001) and (111) substrates. (b) CV comparisons of 16 nm (001) MnFeO₄ and 21 nm (001) Fe₃O₄ under a N_2 atmosphere before RDE experiments.

states, as the Fe^{3+} satellite is less pronounced, consistent with previous reports.⁴⁰

ORR Electrocatalysis. Great care was taken in the conversion of MnFe₂O₄ and Fe₃O₄ films into functional electrodes. Nb:STO substrates with MnFe₂O₄ films were mounted on a glassy carbon rotating disk electrode (GC-RDE) using a combination of Ga:In eutectic and Ag paint to make an electrical contact between the GC surface and the backside of the Nb:STO substrate. The entire RDE surface was then sealed with epoxy such that only the spinel oxide surface was exposed. Epoxy coverage was found to be important to the stability of the films. Exposure of the Nb:STO edge resulted in rapid degradation of electrochemical features present in the cyclic voltammogram (Figure S3) and revealed new XPS peaks in the C 1s region consistent with the presence of Sr and Ti atoms (Figure S4). Comparative experiments where the Nb:STO edge was completely covered showed neither electrochemical degradation nor the presence of Sr and Ti peaks from XPS. This result indicates that the MBE films are susceptible to etching at the junction of the film and the substrate, thus covering that the Nb:STO edge, which was found to be critical for film stability during electrochemical experiments.

The CVs of MnFe₂O₄ films were first measured under a N₂ atmosphere to understand their basic electrochemical features. These experiments were performed on the exact films, which were characterized and discussed in the previous section. Figure 6a shows CVs of MnFe₂O₄ for the 6 nm (001), 6 nm (111), and 16 nm (001) films. Despite their different surface roughnesses and thicknesses, the CVs exhibit similar features with two quasi-reversible redox waves at $E_{1/2}$ = 0.96 and 0.62 V vs RHE. Similar features have been observed in CVs of MnFe₂O₄ nanocrystals embedded within carbon black and were assigned to redox chemistry at Mn sites. 11,15 The larger feature at more negative potentials (\sim 0 V vs RHE) has been assigned to redox chemistry at Fe sites. ^{11,22,41} This is consistent with CV data collected here for the 21 nm (001) Fe₃O₄ film, which showed no evidence for Mn redox waves and only showed the more negative feature (Figure 6b). Scan ratedependent studies under a N2 atmosphere revealed surfacebound redox behavior of both Mn waves (Figure S5). The exact assignment of these redox waves is unknown; however, literature evidence suggests several possibilities, including assignment of a Mn^{IV/III} wave at 0.92 V and Mn^{III/II} wave at 0.65 V, 42 although it has been shown to be difficult to oxidize $Mn^{III} \rightarrow Mn^{IV}$ in the spinel structure.²⁹ These oxidation states are most likely stabilized by the formation of M-OH or M-

O(OH) species at the surface of the MnFe₂O₄ film. ⁴³ The second wave (0.65 V) has also been proposed as a Mn^{II/0} wave, which we find unlikely. ¹¹ Studies on bare Nb:STO (Figure S6) also indicated that there was no contribution from the substrate on the electrochemical features observed in Figure 6.

Comparing the 6 nm MnFe $_2$ O $_4$ films, the (001) film was observed to pass more current than the (111) film, even after the CVs were normalized for the geometric surface area ($A_{\rm geo}$). We believe that this is consistent with the larger surface roughness observed by AFM for the (001) film compared with the (111) film such that the electrochemically active surface area (ECSA) of the (001) films was likely larger than the (111) film. Although the exact ECSA is unknown for each film, it was expected to be in the range of 1–1.73 times larger than $A_{\rm geo}$ based on the square pyramidal surface faceting observed by STEM in Figure 4. Using the non-faradaic current observed in Figure 6 and assuming ECSA = $1.73 \times A_{\rm geo}$ as an upper limit resulted in estimates of the specific surface capacitance for MnFe $_2$ O $_4$ of 90–120 μ F cm $^{-2}$ (Supporting Information), consistent with other estimates from the literature.

Finally, we note that scanning the voltage window to more negative potentials resulted in the degradation of the films after repeated cycling. Initial voltammetry studies on the films were restricted to a window less than -0.2 V, as this potential range allowed for stable and reproducible CVs prior to performing electrocatalysis. If scanned more negative than -0.5 V before the introduction of O_2 , film degradation occurred, which we believe was due to proton reduction.

Figure 7 shows CVs of the 16 nm (001) MnFe₂O₄ and 21 nm (001) Fe₃O₄ film saturated with O₂, overlaid with the CV under a N₂ atmosphere. Under an O₂ atmosphere, the film shows a significant increase in current with the second Mn feature at 0.62 V, although a true peak for O₂ reduction is not observed until 0.03 V vs RHE. Similar data was also observed for 6 nm (001) and (111) films (Figure S7). The Fe₃O₄ film also shows an increase in the current upon introduction of O₂. There is no early onset in the current increase as seen with MnFe₂O₄, but a similar onset for the O₂ reduction peak is observed. The total current passing at the O₂ reduction peak for Fe₃O₄ is notably greater than that observed for the MnFe₂O₄ samples.

For a true understanding of the catalytic abilities of MnFe₂O₄ films, RDE experiments were performed. All films were studied at varying rotation rates to perform a Koutecky–Levich analysis (Figure 8). To have comparable numbers to other literature reports of MnFe₂O₄ ORR catalysis, a 20 mV

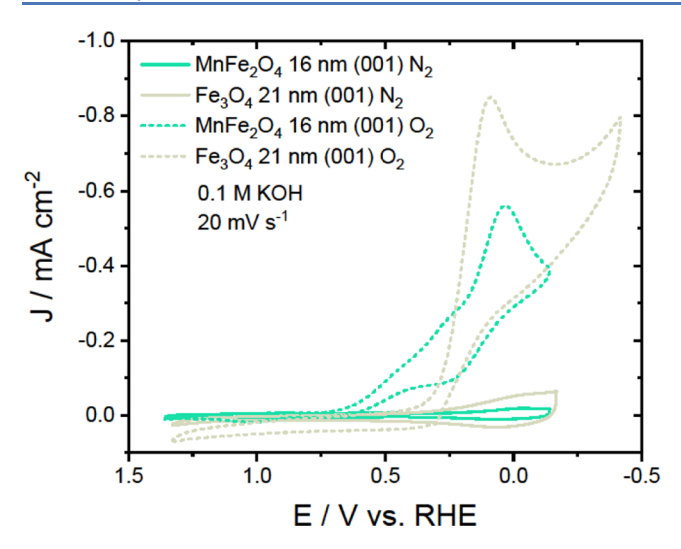


Figure 7. Comparison of MnFe₂O₄ 16 nm (001) and Fe₃O₄ 21 nm (001) under N_2 and O_2 atmospheres during cyclic voltammograms.

s⁻¹ scan rate was used for all rotations. For MnFe₂O₄ and Fe₃O₄ at all rotation rates, it is apparent that the diffusion-limited current is being achieved, as evidenced by the plateau in current density at potentials <0 V. From the polarization curves at 1600 rpm (Figure 8d), the maximum current densities (normalized to $A_{\rm geo}$) observed for 6 nm (001), 6 nm (111), and 16 nm (001) MnFe₂O₄ films were –5.2, –5.3, and –5.3 mA cm⁻², respectively, showing that all films pass the same current at the same rotation rate. The $E_{1/2}$ of the main reduction wave, defined as the potential where half the maximum current is achieved for the 1600 rpm condition, was

 $-0.02~\rm V$ for 6 nm (001), 0 V for 6 nm (111), and 0.04 V for 16 nm (001) MnFe₂O₄. Correction of the RDE data for the upper limit ECSA discussed above resulted in minimal shifts of the $E_{1/2}$ values (Figure S8). The onset potential ($E_{\rm onset}$) for any chemical process must be defined at a specific amount of current passed. Typically, the ORR literature has defined this current as 10 μ A cm⁻², which would result in $E_{\rm onset}$ = 0.74, 0.68, and 0.77 V for 6 nm (001), 6 nm (111), and 16 nm (001) films, respectively. Notably, this onset is inconsistent with the large increase in current observed at potentials <0.25 V. The onset of the large wave was measured for 500 μ A cm⁻² to yield $E_{\rm onset}$ = 0.12 V for 6 nm (001), 0.15 V for 6 nm (111), and 0.22 V for 16 nm (001).

The Fe₃O₄ film showed similar ORR activity in the Fe region (<0.25 V) and virtually no catalysis in the Mn region (>0.25 V). Specifically, at 1600 rpm, the maximum current value reached was 5.5 mA cm⁻² with $E_{\rm onset}$ values of 0.49 V (10 μ A cm⁻²) and 0.18 V (500 μ A cm⁻²). These results clearly differentiate ORR catalysis based on Fe and Mn metal centers with Fe-based catalysis making a much larger contribution. Complete rotation data for Fe₃O₄ 21 nm (001) is shown in Figure S9.

The insets in Figure 8 show Koutecky–Levich plots generated from RDE data at -0.25 V. At large overpotentials, the kinetic limitations of the system are minimized, and linear trends are observed according to the Koutecky–Levich equation (eq 3). Here, n is the number of electrons transferred at the electrode surface, F is Faraday's constant (96,485 C mol⁻¹), C_0 is the saturation concentration of O_2 in 0.1 M KOH at 1 atm of O_2 pressure (1.26 \times 10⁻⁶ mol cm⁻³), D_0 is the diffusion coefficient of O_2 in 0.1 M KOH (1.93 \times 10⁻⁵ cm² s⁻¹), ν is the kinematic viscosity of the 0.1 M KOH electrolyte

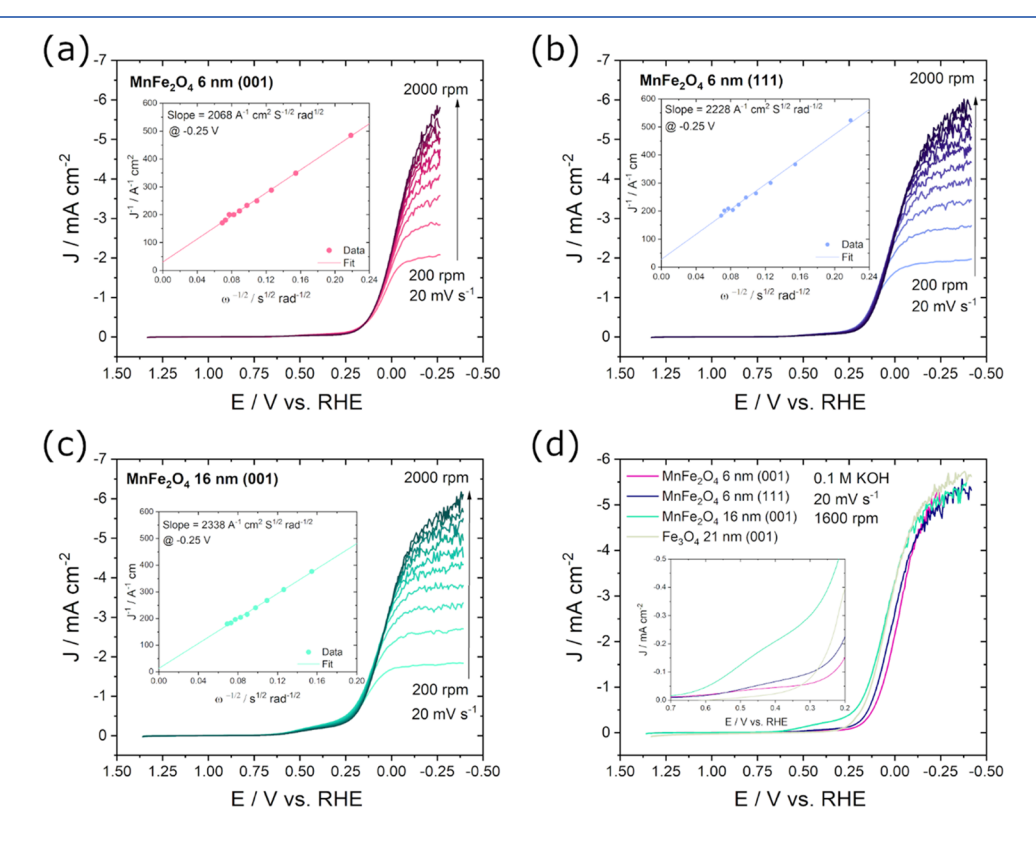


Figure 8. Polarization curves at different rotation rates for (a) 16 nm (001), (b) 6 nm (001), and (c) 6 nm (111) MnFe₂O₄ in 0.1 M KOH saturated with O₂. K-L plots are the inset for each film. (d) Overlay of the polarization curve at 1600 RPM for each MnFe₂O₄ with Fe₃O₄.

 $(1.09 \times 10^{-2} \text{ cm}^2 \text{ s}^{-1})$, and ω is the rotation rate in rad s⁻¹. All Slopes were measured at -0.25 V vs RHE to be 2068, 2228, and 2338 A⁻¹ cm² s^{1/2} rad^{-1/2} for 6 nm (001), 6 nm (111), and 16 nm (001) MnFe₂O₄, respectively. Using the literature values for C_0 , D_0 , and ν , the electron transfer number was calculated from the slope to yield n = 4.2 for 6 nm (001), 3.9 for 6 nm (111), and 3.71 for 16 nm (001). These electron transfer numbers strongly indicate a preference for the direct 4-electron reduction pathway of O_2 as opposed to the 2 × 2-electron pathway that produces H_2O_2 as a byproduct. This is also true for the Fe₃O₄ film, which had an electron transfer value of 3.91. Complete K–L plots from -0.25-0 V are shown in Figure S10.

$$\frac{1}{J} = \frac{1}{J_k} + \frac{1}{J_L} = \frac{1}{nFkC_0} + \frac{1}{0.62nFC_0(D_0)^{2/3}\nu^{-1/6}\omega^{1/2}}$$
(3)

A Koutecky—Levich analysis was also performed with a Pt disk electrode in the same electrode configuration that was used for the spinel films (i.e., with added epoxy) to validate our electrode construction, as well as have comparison K—L slopes. The data for these studies are shown in Figure S11. The calculated electron transfer number calculated for the Pt disk is 4.0.

Following ORR electrocatalysis experiments, the electrolyte was repurged with N_2 to remove O_2 from the system, and CVs were collected over a wider potential range to investigate the stability of MnFe₂O₄ films. For all films, two new redox features in the range that O2 reduction appeared were concomitant with an increase in the non-faradaic current (Figure S12). These features are most likely related to oxidation and reduction of Fe sites in the MnFe₂O₄ structure. Either the exposure to the alkaline conditions of the electrolyte or the process of performing ORR changed the film surface. In particular, the CV for 16 nm (001) looked significantly different than that collected under a N2 atmosphere prior to electrocatalysis, as a sharp peak arises that is present both under N2 and O2 atmospheres. After completion of these experiments, the 16 nm (001) film was removed from the solution for repeat electrochemical analysis. As shown in Figure S13, the film was significantly less catalytic in the second electrochemical experiment than it was upon initial electrocatalysis.

XPS, XRD, and STEM characterization studies of the films were performed after catalysis to explore how catalysis was affecting the film structure. Due to significant changes in Fe and Mn 2p spectra shapes after exposure to air, the stoichiometry of the post-catalysis samples could not reliably be determined. However, from XPS, we observed no significant change in the Mn or Fe valence, indicating that the spinel structure of the film remained intact (Figure S14). This is further verified by XRD on the films after catalysis, which shows no apparent changes in out-of-plane lattice parameters (Figure S15). STEM data showed that after catalysis experiments, some changes in the sample morphology are evident, particularly an increase in bridging between islands (Figure S16). However, no obvious changes in composition or intermixing occurred.

DISCUSSION

The active site for metal oxide ORR catalysis depends significantly on the coordination environment of the metal

cation, its oxidation state, and exposure of that active site at the film surface. In several studies of the ORR on spinel oxide nanocrystals, an investigation of faceting has been performed to understand which crystal faces are best for catalysis.44-For a spinel structure, the surface could consist of two different metals, in two different oxidation states, in two different coordination sites. This can be further complicated if the spinel structure is inverted, so the determination of the active cation and coordination is useful for catalyst design. It has been found that the {111} facet of spinels is more active than that of {001},⁴⁶ and we expected this to be reflected in our studies of MBE films by choosing (001) and (111) Nb:STO substrates to dictate surface termination of the spinel. However, due to the lattice mismatch between the spinel films and Nb:STO substrate as well as the lower surface energy of the spinel {111} facets, ⁴⁹ we observe the growth of {111} faceted islands on MnFe2O4 and Fe3O4 films as evidenced by RHEED and STEM. The island growth pattern observed for MnFe₂O₄ and Fe₃O₄ spinels is also consistent with what has been observed for Fe₃O₄ and CoFe₂O₄ growth on a perovskite substrate. ^{27,35,50} Interestingly, the growth of MnFe₂O₄ on (111)oriented Nb:STO substrates also displayed an island growth pattern according to RHEED images but with lower surface roughness than films grown on (001) Nb:STO. Such island growth is likely due to lattice mismatch between the (111) planes of Nb:STO and MnFe₂O₄, given that surface energetics no longer drive the formation of faceted pyramids along this orientation. The bridges between the islands on the (001) films are (001) faceted, whereas only (111) facets are exposed on the (111) grown MnFe₂O₄.

The choice of Nb:STO substrates in this work was important, as it allowed for electrical contact to be made with MnFe₂O₄ across the entire film area through a backside contact with Nb:STO and the underlying GC electrode. With a nonconductive substrate material such as MgAl₂O₄ or MgO, uniform planar growth of MnFe₂O₄ (i.e., nonisland growth) would be expected; however, electrical contact would need to be made to the front face of the MnFe₂O₄ film. This strategy was recently reported for a series of Co_xFe_{3-x}O₄ spinels grown by MBE and studied as the ORR catalyst; however, the diffusion-limited current was not observed.²⁷ This strategy requires the MBE film to be conductive across the lateral face to transport charge from the contact point at the edge of the film to the exposed face in the center. The method of backside contact employed here shows a clear diffusion-limited current for all electrodes. This suggests that this electrode architecture may be important in the study of MBE spinel catalysts for the ORR and emphasizes the need for conductive substrates with better lattice matching to spinel oxides to achieve planar growth of specific surface facets.

From our ORR study of MnFe₂O₄ and Fe₃O₄ MBE films, high selectivity for the 4e⁻ reduction of O₂ to OH⁻ was determined based on electron transfer numbers (n = 3.7-4.2) obtained from Koutecky–Levich analyses. The 4e⁻ reduction process has been reported for MnFe₂O₄ nanocrystals by Zhu et al. and Zhou et al.; however, Yang et al. have reported an electron transfer value of only 2.6, indicating lower selectivity and more H₂O₂ production. Differences in electron transfer numbers notwithstanding, the significant difference between our study and those of nanocrystalline MnFe₂O₄ lies is the large overpotential required to achieve the diffusion-limited current, which when measured at the $E_{1/2}$ for the diffusion-limited wave is 0.8–1.0 V more negative than what has

previously been reported for MnFe $_2$ O $_4$ nanocrystals. These studies have routinely observed $E_{1/2}$ and $E_{\rm onset}$ values at potentials coincident with the Mn-based redox events, as measured under a N $_2$ atmosphere. Indeed, we did observe a small amount of ORR catalysis at the Mn waves; however, a significant catalytic current was not passed until the Fe-based redox feature was accessible.

We believe the large difference in overpotential between the present study of MBE films and nanocrystalline materials is due to a combination of a low density of Mn at the electrode surface and poor conductivity through the film. Further investigation of the CV data collected under a N2 atmosphere provides support for this argument. Integration of both Mn redox waves yields total charge densities of 21.7, 9.0, and 24.3 μ C cm⁻² for the 6 nm (001), 6 nm (111), and 16 nm (001) films, respectively. The assignment of the two Mn redox waves is unclear from the literature of MnFe₂O₄; however, we believe that they are most likely $1e^-$ processes (e.g., $Mn^{III} \rightarrow \, Mn^{II})$ corresponding to distinct atomic environments at the electrode surface. Zhou et al. showed that increasing the Mn content from x = 0.5 to 2.5 for Mn_xFe_{3-x}O₄ nanocrystals resulted in a decrease in current at the 0.65 V wave and an increase in current at the 0.92 V wave. 15 This behavior suggests two environments of Mn for each redox event as opposed to sequential reduction of the same Mn atom. Therefore, the total charge density can be taken to represent the total Mn density at the surface, assuming 1e processes. We interpret the greater charge densities measured for films grown on (001) vs (111) substrates as a reflection of the larger surface roughness measured by AFM, 3.2 ± 0.5 vs 1.0 ± 0.5 nm, respectively.

A calculation of the total surface atomic density (Mn + Fe sites) for the (111) facet of MnFe₂O₄ yields a charge density of 154 μ C cm⁻² (Figure S17, Table S3). Comparison of this value with the measured charge densities of MnFe₂O₄ films shows the percent coverage of Mn sites to be 14.1, 5.8, and 15.8% for 6 nm (001), 6 nm (111), and 16 nm (001) films, respectively. An ideal (111) surface should be 67% Mn for a normal structure or 33% for an inverse structure, indicating that the MBE films studied here are deficient in available Mn sites needed to catalyze the ORR at lower overpotentials.

The question that remains is: why are these films deficient in Mn at the surface? XPS data showed Mn/Fe ratios close to 0.5, as would be expected for MnFe₂O₄. Therefore, large Mn deficiency throughout the crystal structure should not be the cause. One simple reason could be that the electrode surface is not entirely {111} terminated. STEM results clearly showed {111}-faceted islands separated by regions of (001) bridges. For the STEM sample that was analyzed, islands were as much as 20 nm apart from one another, reducing the exposed MnFe₂O₄ surface area by 50–75%. Islands are also known to truncate to (001) surfaces to reduce the overall surface area, which could further reduce the area of {111} facets. This was not directly observed in STEM data for our sample; however, we were only able to observe a limited number of islands.

As alluded to above, the degree of inversion could also be a factor in determining the Mn site density as this affects tetrahedral vs octahedral site occupation. In a previous study of MnFe₂O₄ grown via MBE, inversion was found to be 20%,³⁰ in agreement with bulk measurements.⁵² Although we did not measure the extent of inversion here, based on a value of 20%, we would expect the (111) surface to contain 60% Mn distributed over both tetrahedral and octahedral sites. The measured values reported above are much less than this ideal

scenario, suggesting that inversion may result in Mn occupation of octahedral sites, which are below the surface. This would yield a {111} surface predominately Fe in character, consistent with the observed electrocatalysis. However, based on the low resolution of the STEM-EDS data along the {111} surface, it is difficult to make a hard conclusion on this claim.

Inversion is also strongly linked to conductivity in spinel ferrites. 52 Yang et al. chose $\mathrm{Fe_3O_4}$ to examine spinel MBE ORR electrocatalysis as it is a highly conductive metal oxide due to its inverse structure having a mixture of $\mathrm{Fe^{II}}$ and $\mathrm{Fe^{III}}$ in octahedral sites, which allows for efficient charge hopping through edge-shared octahedra. However, the introduction of a small amount of $\mathrm{Co^{II}}$ into the spinel structure decreased the conductivity of the films significantly, making meaningful elucidation of catalytic properties difficult. The mechanism commonly understood in the literature involves a decrease in the percent inversion such that octahedral sites have a decrease in the mixture of oxidation states (i.e., more $\mathrm{Fe^{III}}$), which promotes charge hopping.

The CV data collected under an O2 atmosphere without stirring clearly shows that Fe₃O₄ passed more current than MnFe₂O₄, suggesting that Fe₃O₄ is more conductive than MnFe₂O₄. Assuming 20% inversion for MnFe₂O₄, 90% of octahedral sites would be Fe^{III}, resulting in lower conductivity than Fe₃O₄ (50% Fe^{III}). Interestingly, we note that the overpotential for ORR catalysis and the diffusion-limited current observed during rotating experiments was very similar between MnFe₂O₄ and Fe₃O₄, which suggests that communication between surface Fe and the bulk is sufficient to perform catalysis even with Mn in the structure. It is hypothesized that charge hopping in mixed spinels is more likely to occur between cations of the same identity (i.e., Fe^{III} → Fe^{II} or Mn^{III} → Mn^{II}), ³¹ which supports the consistently high activity of Febased catalysis between Fe₃O₄ and MnFe₂O₄. The low catalytic activity of Mn may therefore be due to lower conductivity to Mn specific sites at the surface, which would be controlled by Fe → Mn electron transfer. Small differences in inversion and conductivity may also explain the slightly larger catalytic current observed at Mn sites for 16 nm (001) vs 6 nm (001) despite both having a similar Mn site surface density.

For nanocrystalline materials, poor conductivity is overcome by mixing nanocrystals with a conductive carbon material to study ORR reactivity. This has been found to be necessary to achieve lower overpotentials for many different catalysts, including noble metal catalysts and metal oxides. ^{17,18,53-55} In a study of Co₃O₄ spinel by Liang et al., it is very clear that the addition of carbon is necessary for Co₃O₄ to be an effective catalyst. 56 There even seems to be a dependence on the type of the carbon material used, such as graphene or carbon nanotubes, 11 and even the dopant level in the carbon material.⁵⁷ Another common component of the nanocrystal/ carbon composite is Nafion, an ionic polymer for proton transport, that has an effect on the activity and rate constants associated with catalysis. 58,59 The studies presented here attempt to strip away these factors to focus on the fundamental properties of MnFe₂O₄ for ORR catalysis. The use of thin MnFe₂O₄ layers deposited on a uniformly conductive substrate was designed to achieve the same result as the nanocrystal/ carbon composites, where a highly conductive material is used to transport charge and the oxide surface is responsible for catalysis. Even if the lower surface density of Mn sites is accounted for, the observed catalysis at Mn sites for our MBE

films is still lower than what has been observed in $MnFe_2O_4$ nanocrystal/carbon composites, suggesting that carbon supports may play an active role in catalysis.

CONCLUSIONS

In summary, we have studied MnFe₂O₄ and Fe₃O₄ films grown via MBE for ORR catalysis. This is the first study of spinel MBE films for ORR catalysis in which the diffusion-limited current is observed, allowing for the determination of the ORR mechanism to be the 4e⁻ pathway in the case of both materials. We believe that this observation was greatly aided by the electrode architecture, which employed a conductive Nb:STO substrate for MBE growth, allowing for backside contact to be made with the spinel films. Importantly, the 4e⁻ pathway is only observed at potentials consistent with Fe-based redox activity. In the case of MnFe₂O₄, catalysis at Mn-based redox features was much lower than what has been observed for nanocrystalline/carbon composite electrodes. This behavior could result from multiple factors, including a low density of Mn surface sites and poor conductivity through the MnFe₂O₄ film. The low density of Mn surface sites due to island growth highlights the need for conductive, single-crystal spinel substrates for MBE growth. The production of such materials would enable planar spinel catalyst films to be synthesized with control of surface termination (i.e., {111} vs {001}). The studies reported here are among the first of their kind and further research in this area will continue to gain definitive knowledge on the ORR activity of spinel oxides.

ASSOCIATED CONTENT

Supporting Information

The Supporting Information is available free of charge at https://pubs.acs.org/doi/10.1021/acscatal.1c05172.

RHEED, AFM, XRR, EDS, and XPS characterization of epitaxial films; cyclic voltammograms and Koutecky—Levich analysis of ORR electrocatalysis; ECSA, specific surface capacitance, and surface charge density calculations (PDF)

AUTHOR INFORMATION

Corresponding Authors

Ryan B. Comes — Department of Physics, Auburn University, Auburn, Alabama 36849, United States; orcid.org/0000-0002-5304-6921; Email: ryan.comes@auburn.edu

Byron H. Farnum – Department of Chemistry and Biochemistry, Auburn University, Auburn, Alabama 36849, United States; orcid.org/0000-0001-9152-1909; Email: farnum@auburn.edu

Authors

Alexandria R. C. Bredar – Department of Chemistry and Biochemistry, Auburn University, Auburn, Alabama 36849, United States; orcid.org/0000-0003-4599-8559

Miles D. Blanchet – Department of Physics, Auburn University, Auburn, Alabama 36849, United States

Andricus R. Burton — Department of Chemistry and Biochemistry, Auburn University, Auburn, Alabama 36849, United States; Oorcid.org/0000-0002-4121-5513

Bethany E. Matthews — Energy and Environment Directorate, Pacific Northwest National Laboratory, Richland, Washington 99352, United States; orcid.org/0000-0001-7193-2583

Steven R. Spurgeon — Energy and Environment Directorate, Pacific Northwest National Laboratory, Richland, Washington 99352, United States; Department of Physics, University of Washington, Seattle, Washington 98195, United States; Orcid.org/0000-0003-1218-839X

Complete contact information is available at: https://pubs.acs.org/10.1021/acscatal.1c05172

Author Contributions

¹A.R.C.B. and M.D.B. contributed equally.

Notes

The authors declare no competing financial interest.

ACKNOWLEDGMENTS

A.R.C.B, M.D.B., A.R.B., R.B.C, and B.H.F. acknowledge support from the National Science Foundation Division of Materials Research through grant NSF-DMR-1809847. Additionally, A.R.C.B, M.D.B., and A.R.B. acknowledge support from the Alabama EPSCOR Graduate Research Scholars program. HRXRD was performed with a Rigaku SmartLab instrument purchased with support from the National Science Foundation Major Research Instrumentation program through grant NSF-DMR-2018794. B.E.M. and S.R.S. were supported by the Chemical Dynamics Initiative/Investment at Pacific Northwest National Laboratory (PNNL). PNNL is a multiprogram national laboratory operated for the U.S. Department of Energy (DOE) by Battelle Memorial Institute under Contract No. DE-AC05-76RL01830. STEM sample preparation was performed in the Environmental Molecular Sciences Laboratory (EMSL), a national scientific user facility sponsored by the Department of Energy's Office of Biological and Environmental Research and located at PNNL. STEM imaging was performed in the Radiological Microscopy Suite (RMS), located in the Radiochemical Processing Laboratory (RPL) at PNNL.

■ REFERENCES

- (1) Gasteiger, H. A.; Marković, N. M. Just a Dream—or Future Reality? Science 2009, 324, 48-49.
- (2) Ge, X.; Sumboja, A.; Wuu, D.; An, T.; Li, B.; Goh, F. W. T.; Hor, T. S. A.; Zong, Y.; Liu, Z. Oxygen Reduction in Alkaline Media: From Mechanisms to Recent Advances of Catalysts. ACS Catal. 2015, 5, 4643–4667.
- (3) Ma, R.; Lin, G.; Zhou, Y.; Liu, Q.; Zhang, T.; Shan, G.; Yang, M.; Wang, J. A Review of Oxygen Reduction Mechanisms for Metal-Free Carbon-Based Electrocatalysts. *npj Comput. Mater.* **2019**, *S*, No. 78.
- (4) Cheng, F.; Chen, J. Metal—Air Batteries: From Oxygen Reduction Electrochemistry to Cathode Catalysts. *Chem. Soc. Rev.* **2012**, *41*, 2172—2192.
- (5) Zhao, Q.; Yan, Z.; Chen, C.; Chen, J. Spinels: Controlled Preparation, Oxygen Reduction/Evolution Reaction Application, and Beyond. *Chem. Rev.* **2017**, *117*, 10121–10211.
- (6) Yang, Y.; Xiong, Y.; Holtz, M. E.; Feng, X.; Zeng, R.; Chen, G.; DiSalvo, F. J.; Muller, D. A.; Abruña, H. D. Octahedral Spinel Electrocatalysts for Alkaline Fuel Cells. *Proc. Natl. Acad. Sci. U.S.A.* **2019**, *116*, 24425–24432.
- (7) Vielstich, W.; Lamm, A.; Gasteiger, H. Handbook of Fuel Cells. Fundamentals, Technology, Applications.; Wiley, 2003; Vol. 1, pp 221–225.
- (8) Wu, G.; Wang, J.; Ding, W.; Nie, Y.; Li, L.; Qi, X.; Chen, S.; Wei, Z. A Strategy to Promote the Electrocatalytic Activity of Spinels for Oxygen Reduction by Structure Reversal. *Angew. Chem., Int. Ed.* **2016**, *55*, 1340–1344.

- (9) Zhou, Y.; Xi, S.; Wang, J.; Sun, S.; Wei, C.; Feng, Z.; Du, Y.; Xu, Z. J. Revealing the Dominant Chemistry for Oxygen Reduction Reaction on Small Oxide Nanoparticles. *ACS Catal.* **2018**, *8*, 673–677.
- (10) Wang, C.; Daimon, H.; Sun, S. Dumbbell-like Pt-Fe3O4 Nanoparticles and Their Enhanced Catalysis for Oxygen Reduction Reaction. *Nano Lett.* **2009**, *9*, 1493–1496.
- (11) Zhu, H.; Zhang, S.; Huang, Y.-X.; Wu, L.; Sun, S. Monodisperse MxFe3–XO4 (M = Fe, Cu, Co, Mn) Nanoparticles and Their Electrocatalysis for Oxygen Reduction Reaction. *Nano Lett.* **2013**, *13*, 2947–2951.
- (12) Li, P.; Ma, R.; Zhou, Y.; Chen, Y.; Zhou, Z.; Liu, G.; Liu, Q.; Peng, G.; Liang, Z.; Wang, J. In Situ Growth of Spinel CoFe 2 O 4 Nanoparticles on Rod-like Ordered Mesoporous Carbon for Bifunctional Electrocatalysis of Both Oxygen Reduction and Oxygen Evolution. *J. Mater. Chem. A* 2015, 3, 15598–15606.
- (13) Zhao, X.; Fu, Y.; Wang, J.; Xu, Y.; Tian, J.-H.; Yang, R. Ni-Doped CoFe2O4 Hollow Nanospheres as Efficient Bi-Functional Catalysts. *Electrochim. Acta* **2016**, *201*, 172–178.
- (14) Khilari, S.; Pradhan, D. MnFe2O4@nitrogen-Doped Reduced Graphene Oxide Nanohybrid: An Efficient Bifunctional Electrocatalyst for Anodic Hydrazine Oxidation and Cathodic Oxygen Reduction. *Catal. Sci. Technol.* **2017**, *7*, 5920–5931.
- (15) Zhou, Y.; Xi, S.; Wang, J.; Sun, S.; Wei, C.; Feng, Z.; Du, Y.; Xu, Z. J. Revealing the Dominant Chemistry for Oxygen Reduction Reaction on Small Oxide Nanoparticles. *ACS Catal.* **2018**, *8*, 673–677.
- (16) Xiong, Y.; Yang, Y.; Feng, X.; DiSalvo, F. J.; Abruña, H. D. A Strategy for Increasing the Efficiency of the Oxygen Reduction Reaction in Mn-Doped Cobalt Ferrites. *J. Am. Chem. Soc.* **2019**, *141*, 4412–4421.
- (17) Poux, T.; Napolskiy, F. S.; Dintzer, T.; Kéranguéven, G.; Istomin, S. Ya.; Tsirlina, G. A.; Antipov, E. V.; Savinova, E. R. Dual Role of Carbon in the Catalytic Layers of Perovskite/Carbon Composites for the Electrocatalytic Oxygen Reduction Reaction. *Catal. Today* **2012**, *189*, 83–92.
- (18) Kim, J. H.; Cheon, J. Y.; Shin, T. J.; Park, J. Y.; Joo, S. H. Effect of Surface Oxygen Functionalization of Carbon Support on the Activity and Durability of Pt/C Catalysts for the Oxygen Reduction Reaction. *Carbon* **2016**, *101*, 449–457.
- (19) Markovic, N. M.; Gasteiger, H. A.; Ross, P. N. Oxygen Reduction on Platinum Low-Index Single-Crystal Surfaces in Sulfuric Acid Solution: Rotating Ring-Pt(Hkl) Disk Studies. *J. Phys. Chem. A* 1995, 99, 3411–3415.
- (20) Climent, V.; Marković, N. M.; Ross, P. N. Kinetics of Oxygen Reduction on an Epitaxial Film of Palladium on Pt(111). *J. Phys. Chem. B* **2000**, *104*, 3116–3120.
- (21) Blizanac, B. B.; Ross, P. N.; Marković, N. M. Oxygen Reduction on Silver Low-Index Single-Crystal Surfaces in Alkaline Solution: Rotating Ring DiskAg(Hkl) Studies. *J. Phys. Chem. B* **2006**, *110*, 4735–4741.
- (22) Stoerzinger, K. A.; Lü, W.; Li, C.; Ariando; Venkatesan, T.; Shao-Horn, Y. Highly Active Epitaxial La(1-x)SrxMnO3 Surfaces for the Oxygen Reduction Reaction: Role of Charge Transfer. *J. Phys. Chem. Lett.* **2015**, *6*, 1435–1440.
- (23) May, K. J.; Fenning, D. P.; Ming, T.; Hong, W. T.; Lee, D.; Stoerzinger, K. A.; Biegalski, M. D.; Kolpak, A. M.; Shao-Horn, Y. Thickness-Dependent Photoelectrochemical Water Splitting on Ultrathin LaFeO3 Films Grown on Nb:SrTiO3. *J. Phys. Chem. Lett.* **2015**, *6*, 977–985.
- (24) Lee, D.; Grimaud, A.; Crumlin, E. J.; Mezghani, K.; Habib, M. A.; Feng, Z.; Hong, W. T.; Biegalski, M. D.; Christen, H. M.; Shao-Horn, Y. Strain Influence on the Oxygen Electrocatalysis of the (100)-Oriented Epitaxial La2NiO4+ δ Thin Films at Elevated Temperatures. *J. Phys. Chem. C* **2013**, *117*, 18789–18795.
- (25) Lee, D.; Jacobs, R.; Jee, Y.; Seo, A.; Sohn, C.; Ievlev, A. V.; Ovchinnikova, O. S.; Huang, K.; Morgan, D.; Lee, H. N. Stretching Epitaxial La0.6Sr0.4CoO3 $-\delta$ for Fast Oxygen Reduction. *J. Phys. Chem. C* **2017**, *121*, 25651–25658.

- (26) Kan, D.; Orikasa, Y.; Nitta, K.; Tanida, H.; Kurosaki, R.; Nishimura, T.; Sasaki, T.; Guo, H.; Ozaki, Y.; Uchimoto, Y.; Shimakawa, Y. Overpotential-Induced Introduction of Oxygen Vacancy in La0.67Sr0.33MnO3 Surface and Its Impact on Oxygen Reduction Reaction Catalytic Activity in Alkaline Solution. *J. Phys. Chem. C* 2016, 120, 6006–6010.
- (27) Yang, Y.; Zeng, R.; Paik, H.; Kuo, D.-Y.; Schlom, D. G.; DiSalvo, F. J.; Muller, D. A.; Suntivich, J.; Abruña, H. D. Epitaxial Thin-Film Spinel Oxides as Oxygen Reduction Electrocatalysts in Alkaline Media. *Chem. Mater.* **2021**, 33, 4006–4013.
- (28) Li, Z.; Gao, K.; Han, G.; Wang, R.; Li, H.; Zhao, X. S.; Guo, P. Solvothermal Synthesis of MnFe2O4 Colloidal Nanocrystal Assemblies and Their Magnetic and Electrocatalytic Properties. *New J. Chem.* **2015**, *39*, 361–368.
- (29) Wei, C.; Feng, Z.; Baisariyev, M.; Yu, L.; Zeng, L.; Wu, T.; Zhao, H.; Huang, Y.; Bedzyk, M. J.; Sritharan, T.; Xu, Z. J. Valence Change Ability and Geometrical Occupation of Substitution Cations Determine the Pseudocapacitance of Spinel Ferrite XFe2O4 (X = Mn, Co, Ni, Fe). *Chem. Mater.* **2016**, 28, 4129–4133.
- (30) Matzen, S.; Moussy, J.-B.; Mattana, R.; Bouzehouane, K.; Deranlot, C.; Petroff, F.; Cezar, J. C.; Arrio, M.-A.; Sainctavit, Ph.; Gatel, C.; Warot-Fonrose, B.; Zheng, Y. Epitaxial Growth and Ferrimagnetic Behavior of MnFe\${}_{2}\$O\${}_{4}\$(111) Ultrathin Layers for Room-Temperature Spin Filtering. *Phys. Rev. B* **2011**, *83*, No. 184402.
- (31) Bhargava, A.; Eppstein, R.; Sun, J.; Smeaton, M. A.; Paik, H.; Kourkoutis, L. F.; Schlom, D. G.; Caspary Toroker, M.; Robinson, R. D. Breakdown of the Small-Polaron Hopping Model in Higher-Order Spinels. *Adv. Mater.* **2020**, *32*, No. 2004490.
- (32) Rajagiri, P.; Sahu, B. N.; Venkataramani, N.; Prasad, S.; Krishnan, R. Effect of Substrate Temperature on Magnetic Properties of MnFe2O4 Thin Films. *AIP Adv.* **2018**, *8*, No. 056112.
- (33) Thapa, S.; Paudel, R.; Blanchet, M. D.; Gemperline, P. T.; Comes, R. B. Probing Surfaces and Interfaces in Complex Oxide Films via in Situ X-Ray Photoelectron Spectroscopy. *J. Mater. Res.* **2021**, *36*, 26–51.
- (34) Zheng, H.; Zhan, Q.; Zavaliche, F.; Sherburne, M.; Straub, F.; Cruz, M. P.; Chen, L.-Q.; Dahmen, U.; Ramesh, R. Controlling Self-Assembled Perovskite—Spinel Nanostructures. *Nano Lett.* **2006**, *6*, 1401–1407.
- (35) Comes, R.; Gu, M.; Khokhlov, M.; Liu, H.; Lu, J.; Wolf, S. A. Electron Molecular Beam Epitaxy: Layer-by-Layer Growth of Complex Oxides via Pulsed Electron-Beam Deposition. *J. Appl. Phys.* **2013**, *113*, No. 023303.
- (36) Permien, S.; Hain, H.; Scheuermann, M.; Mangold, S.; Mereacre, V.; Powell, A. K.; Indris, S.; Schürmann, U.; Kienle, L.; Duppel, V.; Harm, S.; Bensch, W. Electrochemical Insertion of Li into Nanocrystalline MnFe2O4: A Study of the Reaction Mechanism. *RSC Adv.* **2013**, *3*, 23001–23014.
- (37) Zhuang, L.; Zhang, W.; Zhao, Y.; Shen, H.; Lin, H.; Liang, J. Preparation and Characterization of Fe3O4 Particles with Novel Nanosheets Morphology and Magnetochromatic Property by a Modified Solvothermal Method. *Sci. Rep.* **2015**, *5*, No. 9320.
- (38) Biesinger, M. C.; Payne, B. P.; Grosvenor, A. P.; Lau, L. W. M.; Gerson, A. R.; Smart, R. StC. Resolving Surface Chemical States in XPS Analysis of First Row Transition Metals, Oxides and Hydroxides: Cr, Mn, Fe, Co and Ni. *Appl. Surf. Sci.* **2011**, *257*, 2717–2730.
- (39) Yamashita, T.; Hayes, P. Analysis of XPS Spectra of Fe2+ and Fe3+ Ions in Oxide Materials. *Appl. Surf. Sci.* **2008**, 254, 2441–2449.
- (40) Chambers, S. A.; Joyce, S. A. Surface Termination, Composition and Reconstruction of Fe3O4(001) and γ -Fe2O3(001). Surf. Sci. 1999, 420, 111–122.
- (41) Sander, M.; Hofstetter, T. B.; Gorski, C. A. Electrochemical Analyses of Redox-Active Iron Minerals: A Review of Nonmediated and Mediated Approaches. *Environ. Sci. Technol.* **2015**, *49*, 5862–5878.
- (42) Wang, Z.; Yang, D.; Sham, T.-K. Effect of Oxidation State of Manganese in Manganese Oxide Thin Films on Their Capacitance Performances. *Surf. Sci.* **2018**, *676*, 71–76.

- (43) Su, H.-Y.; Gorlin, Y.; C Man, I.; Calle-Vallejo, F.; K Nørskov, J.; F Jaramillo, T.; Rossmeisl, J. Identifying Active Surface Phases for Metal Oxide Electrocatalysts: A Study of Manganese Oxide Bi-Functional Catalysts for Oxygen Reduction and Water Oxidation Catalysis. *Phys. Chem. Chem. Phys.* **2012**, *14*, 14010–14022.
- (44) Min, X.; Chen, Y.; Kanan, M. W. Alkaline O2 Reduction on Oxide-Derived Au: High Activity and 4e— Selectivity without (100) Facets. *Phys. Chem. Chem. Phys.* **2014**, *16*, 13601–13604.
- (45) Buvat, G.; Eslamibidgoli, M. J.; Youssef, A. H.; Garbarino, S.; Ruediger, A.; Eikerling, M.; Guay, D. Effect of IrO6 Octahedron Distortion on the OER Activity at (100) IrO2 Thin Film. *ACS Catal.* **2020**, *10*, 806–817.
- (46) Zheng, Y.; Gao, R.; Zheng, L.; Sun, L.; Hu, Z.; Liu, X. Ultrathin Co3O4 Nanosheets with Edge-Enriched {111} Planes as Efficient Catalysts for Lithium—Oxygen Batteries. ACS Catal. 2019, 9, 3773—3782.
- (47) Poulain, R.; Klein, A.; Proost, J. Electrocatalytic Properties of (100)-, (110)-, and (111)-Oriented NiO Thin Films toward the Oxygen Evolution Reaction. *J. Phys. Chem. C* **2018**, 122, 22252–22262
- (48) Maiyalagan, T.; Chemelewski, K. R.; Manthiram, A. Role of the Morphology and Surface Planes on the Catalytic Activity of Spinel LiMn1.SNi0.5O4 for Oxygen Evolution Reaction. ACS Catal. 2014, 4, 421–425
- (49) Mishra, R. K.; Thomas, G. Surface Energy of Spinel. J. Appl. Phys. 1977, 48, 4576–4580.
- (50) Moyer, J. A.; Gao, R.; Schiffer, P.; Martin, L. W. Epitaxial Growth of Highly-Crystalline Spinel Ferrite Thin Films on Perovskite Substrates for All-Oxide Devices. *Sci. Rep.* **2015**, *5*, No. 10363.
- (51) Zheng, H.; Straub, F.; Zhan, Q.; Yang, P.-L.; Hsieh, W.-K.; Zavaliche, F.; Chu, Y.-H.; Dahmen, U.; Ramesh, R. Self-Assembled Growth of BiFeO3–CoFe2O4 Nanostructures. *Adv. Mater.* **2006**, *18*, 2747–2752.
- (52) West, A. R. Solid State Chemistry and Its Applications; John Wiley & Sons, 2014; pp 110-111.
- (53) Zhao, S.; Guo, T.; Fan, J.; Wang, L.; Han, M.; Wang, J.; Wu, Y.; Chen, Y. Versatile Synthesis of Ultrafine Ternary Spinel Oxides/Carbon Nanohybrids toward the Oxygen Reduction Reaction. *Energy Fuels* **2020**, 34, 9069–9075.
- (54) Wu, X.; Niu, Y.; Feng, B.; Yu, Y.; Huang, X.; Zhong, C.; Hu, W.; Li, C. M. Mesoporous Hollow Nitrogen-Doped Carbon Nanospheres with Embedded MnFe2O4/Fe Hybrid Nanoparticles as Efficient Bifunctional Oxygen Electrocatalysts in Alkaline Media. ACS Appl. Mater. Interfaces 2018, 10, 20440–20447.
- (55) Celorrio, V.; Dann, E.; Calvillo, L.; Morgan, D. J.; Hall, S. R.; Fermin, D. J. Oxygen Reduction at Carbon-Supported Lanthanides: The Role of the B-Site. *ChemElectroChem* **2016**, *3*, 283–291.
- (56) Liang, Y.; Li, Y.; Wang, H.; Zhou, J.; Wang, J.; Regier, T.; Dai, H. Co 3 O 4 Nanocrystals on Graphene as a Synergistic Catalyst for Oxygen Reduction Reaction. *Nat. Mater.* **2011**, *10*, 780–786.
- (57) Wang, L.; Sofer, Z.; Pumera, M. Will Any Crap We Put into Graphene Increase Its Electrocatalytic Effect? ACS Nano 2020, 14, 21–25.
- (58) Kocha, S. S.; Zack, J. W.; Alia, S. M.; Neyerlin, K. C.; Pivovar, B. S. Influence of Ink Composition on the Electrochemical Properties of Pt/C Electrocatalysts. *ECS Trans.* **2013**, *50*, 1475.
- (59) Chen, Y.; Zhong, Q.; Li, G.; Tian, T.; Tan, J.; Pan, M. Electrochemical Study of Temperature and Nafion Effects on Interface Property for Oxygen Reduction Reaction. *Ionics* **2018**, *24*, 3905–3914.

